Reactive Blending of Polyamide 6 and Styrene−Acrylonitrile Copolymer: Influence of Blend Composition and Compatibilizer Concentration on Morphology and Rheology

C. Sailer[†] **and U. A. Handge***

Institute of Polymers, Department of Materials, ETH Zurich, Wolfgang-Pauli-Strasse 10, 8093 Zurich, Switzerland

Received January 28, 2008; Revised Manuscript Received March 14, 2008

ABSTRACT: In this article, we report on the influence of reactive compatibilization on the morphological and rheological properties of blends of polyamide 6 (PA 6) and a styrene−acrylonitrile copolymer (SAN). PA 6/SAN blends with two different composition ratios (70/30 and 30/70) and varying concentration of a styrene acrylonitrile maleic anhydride terpolymer (SANMA) were prepared. During melt mixing, the amino end groups of PA 6 react with the maleic anhydride groups of SANMA. The objective of this work is to study the elastic and viscous properties of the blends in shear and elongation as a function of compatibilizer concentration. The composition ratio of the blends (PA 6 or SAN matrix) has a strong influence on the morphology and rheology of the blends, in particular for large SANMA concentrations. We explain this phenomenon by the asymmetric properties of the reactively compatibilized interface which originates from the comblike architecture of the in situ generated interfacial agent. In linear viscoelastic shear oscillations, the reactively compatibilized PA 6/SAN blends with a PA 6 matrix depict for large SANMA concentrations the power laws $G' \propto G'' \propto \omega^n$ with $n \approx 0.58$ whereas the blends with a SAN matrix display a solidlike low frequency behavior. In melt elongation, the extensional viscosity of the PA 6/SAN blends exceed its linear viscoelastic prediction for large SANMA concentrations. Furthermore, our AFM investigations of elongated and subsequently quenched samples reveal that the stretch ratio of spherical SAN domains in the PA 6 matrix increases with SANMA concentration. In recovery, these stretched SAN domains recover more slowly to an isotropic shape when the SANMA concentration was increased.

Introduction

Polymer blending is an economically viable route to tailor new materials with an advantageous combination of end-use properties.[1] However, the inherent immiscibility of most polymer pairs and in a number of cases large values of the interfacial tension counteract a fine dispersion of the components during mixing and lead to coarsening phenomena such as coalescence and Ostwald ripening.[2,3] Furthermore, most immiscible polymer blends suffer from a poor interfacial adhesion which causes inferior mechanical properties in the solid state. In order to overcome these shortcomings, compatibilization is a technologically widely applied routine.[4] A cost-effective technique is to form the compatibilizer in situ by a chemical reaction at the interface during melt mixing. Thereby, a reactive agent which is miscible with one blend component and capable of reacting with complementary groups of the other component is added to the components before blending. During melt mixing the reaction occurs at the interface and generates block or graft copolymers which leads to compatibilization of the two phases.[5] A variety of polymer pairs have been suggested for such an interfacial reaction. The most common reactive pair for commercial blends is polyamide/anhydride which is generally used for the reactive blending of polyamide/polyphenylene ether/styrene-butadiene copolymer, polyamide/ethylene−propylene rubber, and polyamide 6/acrylonitrile−butadiene−styrene copolymer blends.[6]

The influence of the interfacial reaction on the morphology and solid state properties has been extensively investigated for a number of different blends, see, e.g. refs 7–9. Although polymer processing such as extrusion or film blowing is intimately associated with the rheological properties in the melt, a much smaller number of studies focused on the influence of reactive compatibilization on the rheology of polymer blends. In particular, the effect of reactive compatibilization on the morphology development during nonlinear flows has been investigated to much lesser extent.[10] However, such deformation processes play a key role during, e.g., injection molding, and hence they strongly influence the end-use properties of the final product.

The majority of previous rheological studies on reactively compatibilized polymer blends mainly focused on their linear viscoelastic behavior.[11,12] Reactive compatibilization significantly increases the complex modulus of blends of polyamide 6 (PA 6) and styrenic polymers in the low frequency range.[13] Quantitative analysis of the linear viscoelastic data using the extended model of Palierne[14,15] revealed that the physical principles which were established for physically compatibilized blends with preformed compatibilizing agents[16,17] are also valid for in situ compatibilized blends.[18–20] Recently, the morphological and rheological properties of blends of PA 6 and styrene−acrylonitrile copolymer (SAN) which were reactively compatibilized by a styrene−acrylonitrile−maleic anhydride terpolymer (SANMA) and associated with different types of morphology were compared.[21,22] Significant differences in the rheological and morphological behavior between the blends with a PA 6 and a SAN matrix, gave evidence for asymmetric interfacial properties which stem from the comblike architecture of the in situ generated compatibilizing agent.

In our previous works, we focused on blends with different types of morphology where in the one case the concentration of the reactive agent in the SAN phase,[21] and in the other case, the absolute concentration of the reactive agent in the blend[22] was constant. In this work, we studied the influence of compatibilizer concentration on the morphology and rheology of reactively compatibilized PA 6/SAN blends with two different composition ratios of PA 6 and SAN (70/30 and 30/70). Starting from the neat blends, we prepared blends where the concentra-

* Corresponding author. E-mail: ulrich.handge@uni-bayreuth.de.
[†] E-mail: christian.sailer@mat.ethz.ch.

10.1021/ma800200t CCC: $40.75
Published on Web 05/20/2008

Table 1. Properties of the Blend Components[a]

	T_g[b](°C)	T_m[b](°C)	M_n (g/mol)	M_w (g/mol)	M_w/M_n	ρ at 25 °C[c] (g/cm^3)	ρ at 240 °C[c] (g/cm^3)	η_0 at 240 °C (Pa s)
PA 6	53	221	23000	121000	5.3	1.145	0.984	8400
SAN	109		43400	121000	2.8	1.082	0.989	2200

[a] The density is denoted by ρ and the zero shear rate viscosity by η_0. [b] Determined from DSC thermograms (heating rate: 10 K/min, second heating scan). [c] Determined by the buoyancy method and *pVT* measurements.

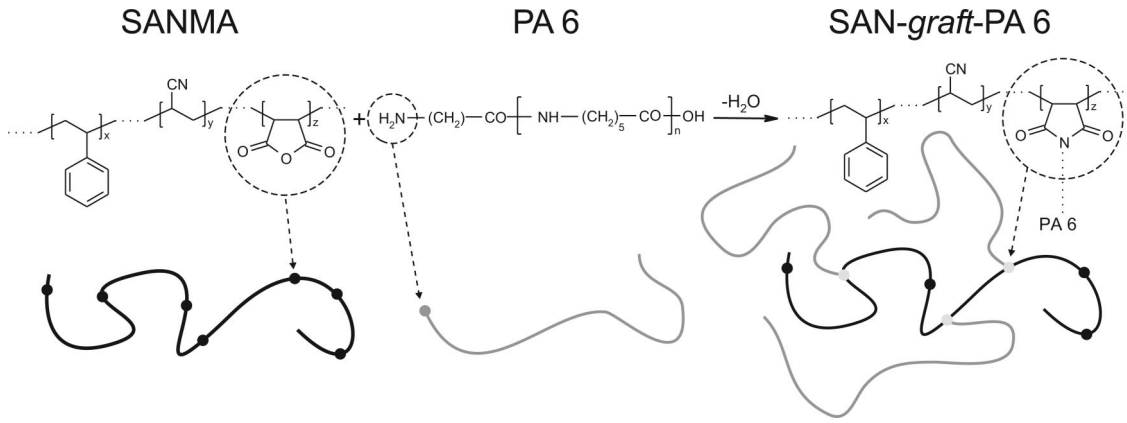

Figure 1. Compatibilizing reaction between SANMA and PA 6. The maleic anhydride groups of SANMA react with the amino end groups of the PA 6 chains such that a multigrafted terpolymer is formed.

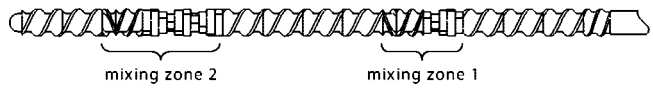

Figure 2. Configuration of the screws of the twin screw extruder. The screw diameter was 25 mm and the L/D ratio was 22. The temperature of extrusion was 240 °C.

Table 2. Composition of the PA 6/SAN/SANMA Blends with 70 wt % PA 6 (PA 70 series)

abbr	$\phi_{PA\,6}$ (wt %)	ϕ_{SAN} (wt %)	ϕ_{SANMA} (wt %)	c_{NH_2} (mmol/kg)	c_{MA} (mmol/kg)	r_{MA/NH_2}
PA70n	70	30	0	30.43	0	0
PA70s	70	29.4	0.6	30.43	1.29	0.04
PA70m	70	28.0	2.0	30.43	4.29	0.14
PA70l	70	26.6	3.4	30.43	7.29	0.24
PA70h	70	25.2	4.8	30.43	10.29	0.34

Table 3. Composition of the PA 6/SAN/SANMA Blends with 30 wt % PA 6 (PA 30 series)

abbr	$\phi_{PA\,6}$ (wt %)	ϕ_{SAN} (wt %)	ϕ_{SANMA} (wt %)	c_{NH_2} (mmol/kg)	c_{MA} (mmol/kg)	r_{MA/NH_2}
PA30n	30	70	0	13.04	0	0
PA30s	30	69.4	0.6	13.04	1.29	0.10
PA30m	30	68.0	2.0	13.04	4.29	0.33
PA30l	30	66.6	3.4	13.04	7.29	0.56
PA30h	30	65.2	4.8	13.04	10.29	0.79

tion of the reactive agent in the SAN phase was incrementally increased. Experiments in linear viscoelastic oscillatory shear flow as well as in nonlinear uniaxial elongational flow (followed by a recovery interval) were performed in order to analyze the elastic and viscous properties as a function of the degree of compatibilization. Furthermore, we aimed to elucidate the asymmetric nature of the compatibilized interface by elaborating the differences between the blends with a PA 6 and a SAN matrix, respectively. PA 6/SAN blends are related to commercially important PA 6/ABS blends. In contrast to their commercial counterparts, PA 6/SAN blends do not contain rubber particles in the SAN phase. The strong effect of the rubber particles on the rheology of the blends would mask the influence of the compatibilizing reaction.

Experimental Section

Materials. The blend components were commercial grades of PA 6 and SAN with 35 wt % of acrylonitrile (BASF AG, Ludwigshafen, Germany; see Table 1 for details). A styrene−acrylonitrile−maleic anhydride random terpolymer (SANMA) with a number average molecular weight $M_n = 52\,000$ g/mol and a weight average molecular weight $M_w = 115\,000$ g/mol was used as the reactive agent. The terpolymer is composed of 69 wt % styrene, 29 wt % acrylonitrile, and 2.0 wt % of maleic anhydride (MA) such that on average approximately 20 MA groups were randomly located on the backbone of one terpolymer chain. During melt mixing the MA groups are capable of reacting with the amino end groups of PA 6. The grafting reaction takes place in the initial stage of mixing and generates comblike SANMA multigrafted PA 6 polymers at the interface between the blend components; see Figure 1.[23–25]

The blends were prepared in two steps. The first step involved the melt mixing of SANMA into the SAN grade and was performed by the supplier. Then, after drying the pellets in vacuum for 7 days at 80 °C, the PA 6 and the SAN grade (containing SANMA) were melt blended using a corotating twin-screw extruder (Brabender, Duisburg, Germany). The screws had a modular design with two mixing zones that consist of reverse conveyor elements and kneading elements (Figure 2). The screw diameter was 25 mm and the L/D ratio 22. The number of screw rotations was set to 50 min $^{-1}$, and the extrusion temperature

was 240 °C. By putting a metal plate in the vicinity of the die outflow the extruded strand was piled up to small pieces of roughly 15 g, which were subsequently compression molded in vacuum at 240 °C to rectangular plates of dimensions 100 × 70 × 2 mm^3. The samples for rheological experiments were prepared by cutting these plates into cylindrical samples with a diameter of 22 mm and a thickness of 2 mm for shear experiments and into rectangular samples of dimensions 56 × 7 × 2 mm^3 for elongation experiments. In this study, two different blend series with a constant concentration of PA 6 were prepared. The blends which contain 70 wt % of PA 6 are denoted by PA70, and the blends which contain 30 wt % of PA 6 are indicated by PA30. For each blend series, neat blends containing no terpolymer (n), and blends with an absolute SANMA concentration of 0.6 wt % (s), 2.0 wt % (m), 3.4 wt % (l), and 4.8 wt % (h) were prepared. The composition of the blends including the concentration c_{NH_2} of amino end groups, the concentration c_{MA} of maleic anhydride, and the ratio r_{MA/NH_2} of amino end group to maleic anhydride concentration are listed in Table 2 for the PA70 series and in Table 2 for the PA30 series.

Rheology. Linear viscoelastic measurements were performed using the shear rheometer UDS 200 (Physica, Stuttgart, Germany) in a parallel plate geometry with 25 mm in diameter. The experiments were conducted at 240 °C in a nitrogen atmosphere, and the shear amplitude was $\gamma_0 = 0.03$. Uniaxial elongation and subsequent recovery experiments were performed at 240 °C using the RME.[26] The experiments were conducted for two different Hencky strain rates $\dot{\varepsilon}_0$ of 0.1 and 0.3 s^{-1}. When the maximum Hencky strain $\varepsilon_{max} = 1.8$ (which corresponds to the stretch ratio $\lambda_{max} = \exp(\varepsilon_{max}) = 6.0$) was attained, the sample was cut by a pneumatically driven pair of scissors and could recover freely, see refs 27 and 28 for details.

Morphology. The microstructure of the blends was investigated by atomic force microscopy (AFM) operating in tapping mode. First, cut-offs of the samples were prepared and glued to special holders. In order to obtain plane surfaces, the samples were microtomed under cryo conditions at −120 °C. The measurements were conducted using a Nanoscope IIIa scanning probe microscope (Digital Instruments, Santa Barbara, USA) in the tapping mode. Silicon cantilevers with natural frequencies in the 300 kHz range and a force constant of approximately 42 N/m were used. The images were recorded at moderate to hard tapping conditions which led to a good stiffness related contrast.[29] The resolution of the micrographs was 512 pixels × 512 pixels. Finally, the size of the scan area was adjusted in order to obtain a preferably large scan area with a reasonable resolution of the microstructure. The morphology of the uncompatibilized blends was examined with an Axio Imager.Z1m optical microscope (Zeiss, Oberkochen, Germany) using reflected light differential interference contrast (DIC) optics.

Results

Linear Viscoelastic Properties. The linear viscoelastic material functions of the PA70 series are presented as a function of frequency ω in Figure 3. At large ω, the storage modulus G' of the blends slightly increases with SANMA concentration. On the contrary, the loss modulus G'' almost remains unaffected by the SANMA concentration for $\omega > 100$ rad/s. At low frequencies, the effect of reactive compatibilization becomes much more pronounced. The addition of SANMA increases the complex modulus of the blends at low ω. Remarkably, the blends do not display a distinct shoulder in G' at low ω which would be characteristic for a two-phase emulsion. If the SANMA concentration is increased, the tan δ curve progressively flattens. The storage and the loss modulus of the blend with 4.8 wt % SANMA attain linear curves in the double-logarithmic presentation corresponding to a power-law behavior and the loss tangent tan δ of this blend attains a constant value close to unity for $\omega < 1$ rad/s. This behavior demonstrates that G' and G'' approach equal values over a large frequency range.

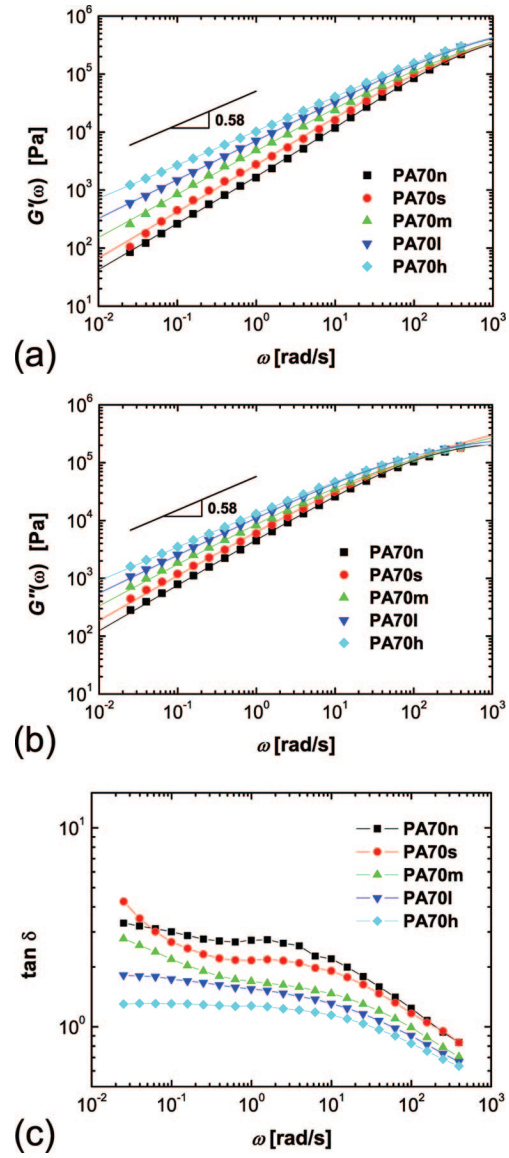

Figure 3. Linear viscoelastic data of the PA70 series: (a) Storage modulus G', (b) loss modulus G'', and (c) loss tangent tan $\delta = G''/G'$ as a function of frequency ω at $T = 240$ °C. The slope of the solid line is 0.58.

Figure 4 presents the linear viscoelastic behavior of the PA30 blends. At large frequencies the PA30 blends display a slight increase of G' and almost unchanged values of G'' with increasing SANMA concentration, similar to the behavior of the PA70 blends. At low ω, the addition of SANMA to blends of SAN and PA 6 leads to an increase of G' and G''. In contrast to the PA70 blends, the storage modulus $G'(\omega)$ of the PA30 blends display a convex shape in the double-logarithmic plot and a local maximum of tan $\delta(\omega)$ for all SANMA concentrations. The convexity of G' is more pronounced and the local maximum of tan δ is shifted to lower values and larger frequencies with increasing SANMA concentration. Within experimental scatter the PA70l and the PA70h blends attain nearly equal dynamic moduli which indicates a saturation-effect at large SANMA concentrations.

In order to calculate the linear viscoelastic prediction $\mu^\circ(t)$ of the transient elongational viscosity $\mu(t)$ of the blends, the fractional Zener model was applied to the experimental data. The complex modulus G^*_{FZM} of this model is given by[30]

$$G^*_{FZM}(\omega) = G_e + G_0 \frac{(i\omega\tau_0)^{\beta_1}}{1 + (i\omega\tau_0)^{\beta_1-\beta_2}} \quad (1)$$

In eq 1, β_1 and β_2 denote the fractional exponents, τ_0 denotes the characteristic time, G_0 denotes the modulus of the fractional elements, and G_e denotes the equilibrium modulus. Hence, the fractional Zener model includes only five parameters. We fitted the complex modulus G^*_{FZM} of this model to the experimental G^* data of the blends. The fits are plotted as solid lines in Figures 3 and 4. Using the fit parameters β_1, β_2, τ_0, G_0, and G_e, the elongational viscosity in the linear viscoelastic regime $\mu^\circ(t)$ is given by[30]

$$\mu^\circ(t) = 3G_e t + 3G_0 \int_0^t (t'/\tau_0)^{-\beta_1} E_{\beta_1-\beta_2,1-\beta_1}[-(t'/\tau_0)^{\beta_1-\beta_2}]\, dt' \quad (2)$$

with the generalized Mittag-Leffler function $E_{\kappa,\nu}[x] = \Sigma_{n=0}^{\infty} x^n/[\Gamma(n\kappa + \nu)]$ and the Gamma function $\Gamma(x)$.

Melt Elongation and Subsequent Recovery Experiments. The transient elongational viscosity

$$\mu(t) = \sigma(t)/\dot{\varepsilon}_0 \quad (3)$$

of the PA70 blends for the strain rates $\dot{\varepsilon}_0 = 0.1$ and 0.3 s^{-1} and its linear viscoelastic prediction $\mu^\circ(t)$ are presented in Figure 5. The elongational viscosity of the blends increases with time and SANMA concentration. For the PA70n, PA70s, and PA70m blends, the experimental data agree well with the linear viscoelastic prediction. At large SANMA concentrations, the transient elongational viscosity of the PA70l and the PA70h blends considerably exceeds the linear viscoelastic prediction over almost the entire range of time and deformation, respectively. This effect shows that nonlinear effects set in at small elongational strains for large SANMA concentrations.

Recovery experiments allow one to determine the recoverable deformation and thus to probe the elastic properties of polymeric materials. The transient recovered stretch λ_r is defined by

$$\lambda_r(t') = L_{max}/L(t') \quad (4)$$

where L_{max} denotes the sample length at cutting time t_{max} and $L(t')$ its length at recovery time $t' = t - t_{max}$. The recovered stretch λ_r of the PA70 blends depends in a complex manner on the SANMA concentration for the two applied strain rates, see Figure 6. The PA70n, PA70s, and the PA70m blends display a similar dynamical behavior during recovery. At short recovery times t' the recovered stretch λ_r slightly increases to $\lambda_r \approx 2$ for $\dot{\varepsilon}_0 = 0.1$ s^{-1} and to $\lambda_r \approx 3$ for $\dot{\varepsilon}_0 = 0.3$ s^{-1} and tends to attain an intermediate plateau for 20 s $< t' <$ 200 s. The subsequent increase of λ_r is mostly pronounced for the PA70n and the PA70s blend. The PA70l and PA70h blend depict a significantly different recovery behavior compared to the PA70n, PA70s, and the PA70m blends. The recovered stretch λ_r increases more rapidly and tends to attain a stationary value at $t' > 1000$ s, which corresponds to a nearly completely reversible deformation $\lambda_{max} = 6.0$ in case of the PA70h blend and $\dot{\varepsilon}_0 = 0.3$ s^{-1}.

Figure 7 presents the elongational viscosity of the PA30 series. At small strains a good agreement between the experimental data and the linear viscoelastic prediction $\mu^\circ(t)$ is evident for all SANMA concentrations. At large strains the elongational viscosity increases more rapidly and exceeds the linear viscoelastic prediction. This strain-hardening like behavior is more clearly seen with increasing SANMA concentration. Similar to the linear viscoelastic functions the PA30l and PA30h blends also attain almost equal extensional viscosities. The recovered stretch of the PA30 blends after simple elongation in Figure 8 is strongly influenced by the compatibilizer concentration. For both strain rates the addition of SANMA increases the recovered

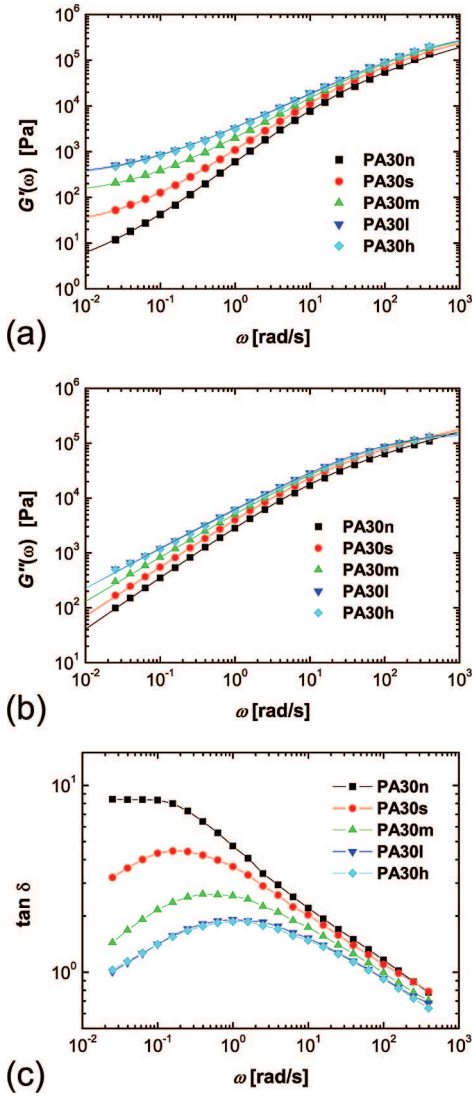

Figure 4. Linear viscoelastic data of the PA30 series: (a) Storage modulus G', (b) loss modulus G'', and (c) loss tangent tan $\delta = G''/G'$ as a function of frequency ω at $T = 240$ °C.

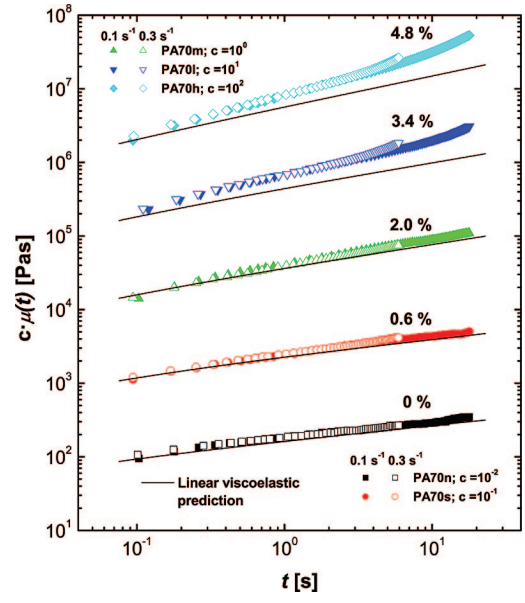

Figure 5. Time-dependent elongational viscosity $\mu(t)$ of the PA70 series at $T = 240$ °C. The Hencky strain rate $\dot{\varepsilon}_0$ (0.1 and 0.3 s^{-1}, respectively) is indicated in the figure. In order to present the data more clearly, the elongational viscosity was shifted by the factor c.

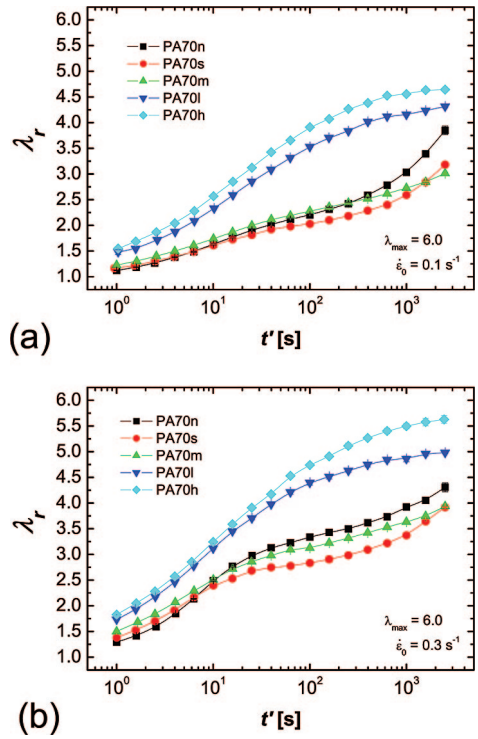

Figure 6. Recovered stretch λ_r as a function of recovery time $t' = t - t_{max}$ for the PA70 series after elongation to the Hencky strain $\varepsilon_{max} = 1.8$ at $T = 240$ °C. The Hencky strain rate was (a) $\dot{\varepsilon}_0 = 0.1$ s^{-1} and (b) $\dot{\varepsilon}_0 = 0.3$ s^{-1}.

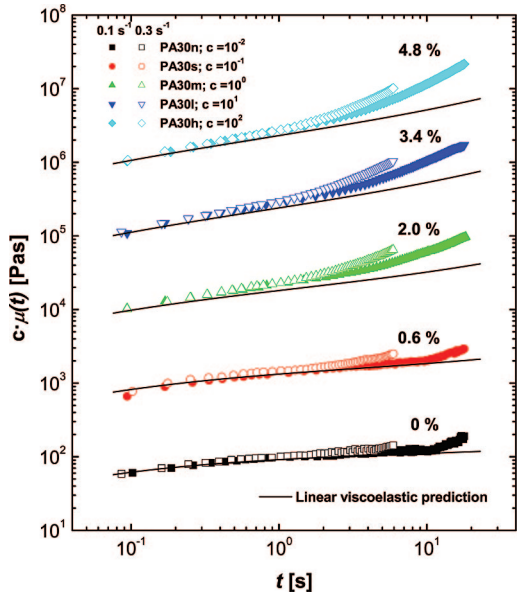

Figure 7. Time-dependent elongational viscosity of the PA30 series at $T = 240$ °C. The Hencky strain rate $\dot{\varepsilon}_0$ (filled symbols 0.1 s^{-1}; open symbols 0.3 s^{-1}) is indicated. The elongational viscosity was shifted by a factor of c.

stretch λ_r of the blends at small t' and changes the recovery dynamics from a convex to a more sigmoidal shape of the λ_r vs log t' curve in the recovery interval of our measurements.

Morphology. The morphology of the uncompatibilized blends is presented in Figure 9. The size of the PA 6 drops of the PA30n blend is larger compared to the SAN domains of the PA70n blend. Furthermore, the large PA 6 domains of the PA30n blend attain a nonspherical shape. These morphological differences can be explained by the different viscosities of the matrix and the dispersed phase which have a 2-fold effect on

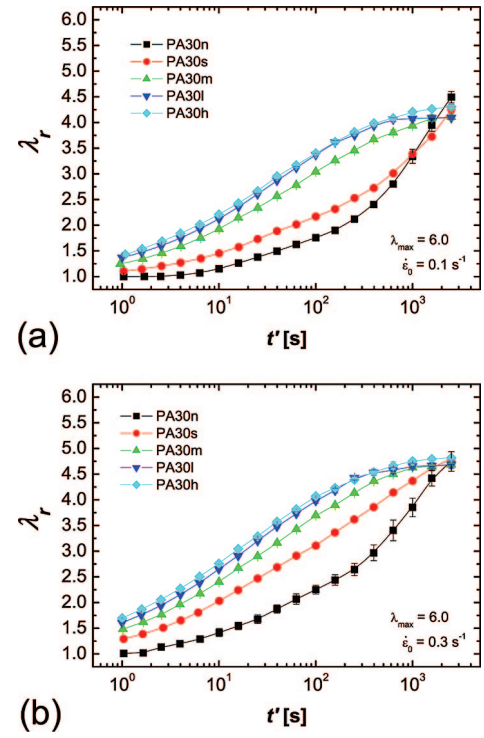

Figure 8. Recovered stretch λ_r versus recovery time $t' = t - t_{max}$ after melt extension to $\varepsilon_{max} = 1.8$ at $T = 240$ °C for the PA30 series. The Hencky strain rate was (a) $\dot{\varepsilon}_0 = 0.1$ s^{-1} and (b) $\dot{\varepsilon}_0 = 0.3$ s^{-1}.

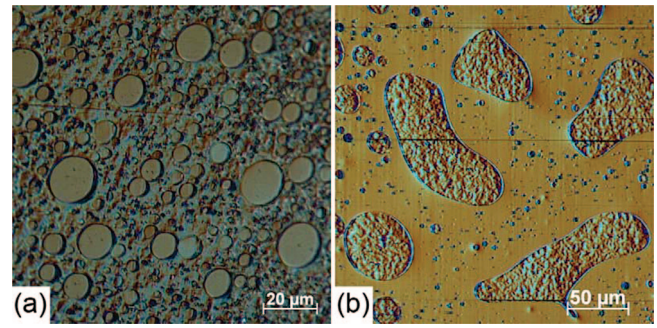

Figure 9. Differential interference contrast (DIC) images of the uncompatibilized (a) PA 6/SAN 70/30 blend (PA70n) and (b) PA 6/SAN 30/70 blend (PA30n).

the morphology: First, a larger matrix viscosity favors a fine dispersion of the minor phase during mixing. Second, larger viscosity ratios promote coalescence by reducing the dimensionless drainage time of the coalescence process.[31] The nonspherical shape of the large PA 6 domains of the PA30n blend is possibly caused by the large time which is necessary for coalesced drops to attain a spherical shape.

The morphology of the reactively compatibilized PA70 blends is shown in Figure 10. For the PA70n, PA70s, and the PA70m blend the measured probability density function $p(r)$ of the drop radius r is plotted in Figure 11. The data can be well represented by the log-normal distribution with the probability density

$$p_{ln}(r) = \frac{1}{\sqrt{2\pi}\sigma_{ln} r} \exp\left\{-\frac{[\ln(r/\kappa_{ln})]^2}{2\sigma_{ln}^2}\right\} \quad (5)$$

which was fitted to the data by adjusting σ_{ln} and κ_{ln}. Furthermore, the correction procedure of Goldsmith[32] was applied in order to determine the number-average $\langle R_n \rangle$ of the drop radius and its volume-average $\langle R_v \rangle$ from the two-dimensional images. Figure 11 demonstrates that reactive compatibilization enor-

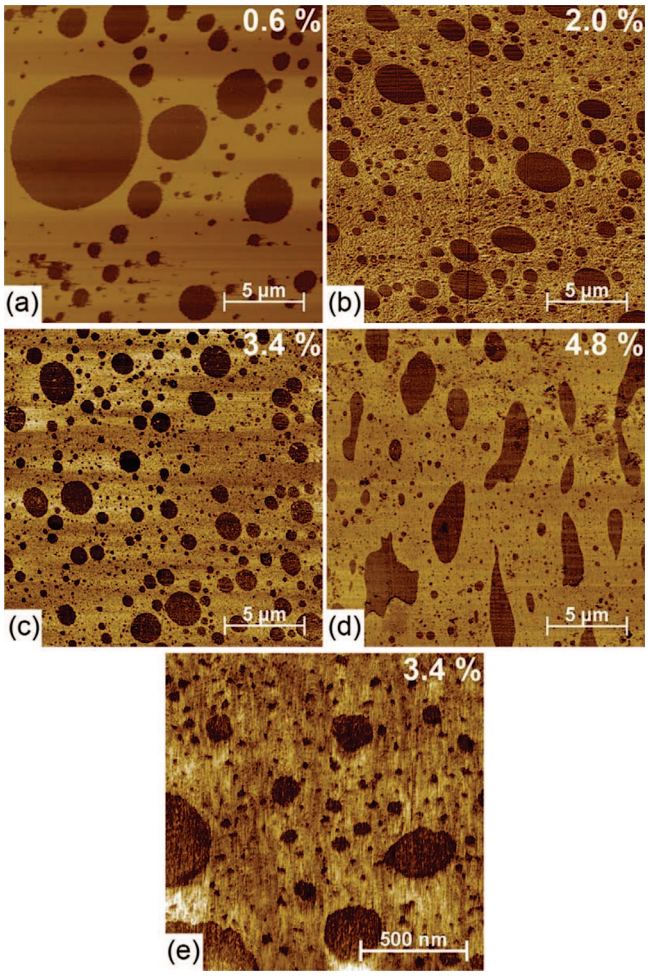

Figure 10. Atomic force micrographs of the compatibilized PA 6/SAN 70/30 blends with (a) 0.6 wt %, (b) 2.0 wt %, (c) 3.4 wt %, and (d) 4.8 wt % SANMA after compression molding. Part e shows the PA 6/SAN 70/30 blend with 3.4 wt % SANMA in a larger magnification.

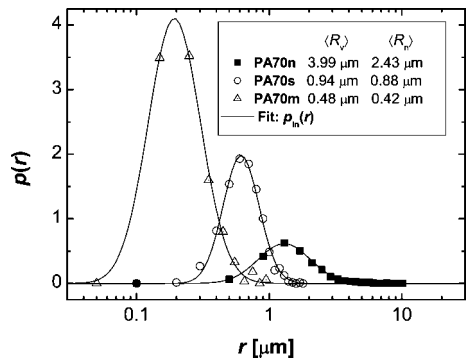

Figure 11. Probability density $p(r)$ of the drop radius for the PA70n, PA70s, and PA70m blends. The log-normal distribution $p_{ln}(r)$ is fitted to the data; see eq 5.

mously reduces the size of the dispersed particles and narrows the distribution of particle sizes up to a SANMA concentration of 2 wt %. The decrease of the particle size can be explained by the inhibition of coalescence in the reactively compatibilized blends.[21] At larger SANMA concentrations a large number of very small SAN domains with a radius in the range of 10−50 nm was formed (see Figure 10e). The preferential formation of these micellar-like SAN domains at larger SANMA concentrations can be attributed to the molecular architecture of the in situ generated grafted SANMA chains. Figure 12

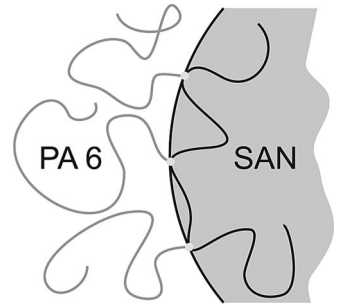

Figure 12. Simplified illustration of one multigrafted SANMA chain at the PA 6/SAN interface. The tendency of the terpolymer backbone to attain a coil-like conformation counteracts a lateral crowding of grafted PA 6 chains in the PA 6 domain. This phenomenon leads to the bending of the interface towards the SAN domain.

illustrates the idealized situation of one comblike multigrafted terpolymer chain at the PA 6/SAN interface. The tendency of the terpolymer backbone to attain a coil-like conformation (gain of entropy) counteracts the repulsion between grafted PA 6 chains at small distances in the PA 6 phase (so-called lateral crowding). These competing effects tend to curve the interface toward the SAN domain.[33–35] At large SANMA concentrations an increasing number of grafted terpolymer chains at the interface enhances the tendency to curve the interface which promotes the formation of very small micellar-like domains. The nonspherical shape of the larger SAN domains of the PA70h blend in Figure 10d indicates that very large relaxation times of the surrounding PA 6 matrix prevent interfacial-tension-driven flow that is necessary to attain a spherical shape of the domain. This phenomenon agrees with the G' and G'' data which reveal that the blends of the PA70 series for very large SANMA concentrations do not behave like a Newtonian fluid at long times. The presence of such long relaxation times can be explained by a substantial portion of grafted PA 6 chains. These PA 6 chains are preferably attached to the micellar-like SAN domains (see Figure 10e) and thereby constrained in their molecular motion.

The morphology of the reactively compatibilized PA30 blends in Figure 13 differs from the microstructure of the PA70 blends in Figure 10. The PA 6 domains generally are nonspherical. At the lowest SANMA concentration (Figure 13a) the characteristic length of the PA 6 domains is roughly 1 order of magnitude smaller than the characteristic size of the PA30n blend (Figure 9(b)) and decreases with SANMA concentration (cf. Figure 13b−d). As shown for the PA30h blend in ref 21, the clusterlike shape of the PA 6 domains result from partial coalescence and agglomeration. The origin of the attractive interaction possibly is the interphase of grafted terpolymer chains which forms a shell on the surface of the PA 6 domains. Because of its chemical composition, this interphase facilitates agglomeration between the PA 6 domains.

Morphology Development during Elongation and Recovery. In order to investigate the influence of reactive compatibilization on the deformation of the morphology, we prepared microscopical specimens from samples that were elongated to $\varepsilon_{max} = 1.8$ with $\dot{\varepsilon}_0 = 0.3\ s^{-1}$ at $T = 240$ °C. The samples were quenched in the rheometer immediately after ε_{max} had been attained and were removed from the apparatus using a quenching tool.[36] Because of the complex shape of the PA 6 domains of the PA30 blends we focus here on the PA70 blends. Figure 14 shows the micrographs of the elongated samples that were taken parallel to the stretching direction. The initially spherical SAN drops are stretched into an ellipsoidal shape. The stretch ratio λ_d of a drop is defined by the ratio of the major axis a of the ellipsoid to the initial particle diameter $2r_0$ and was determined

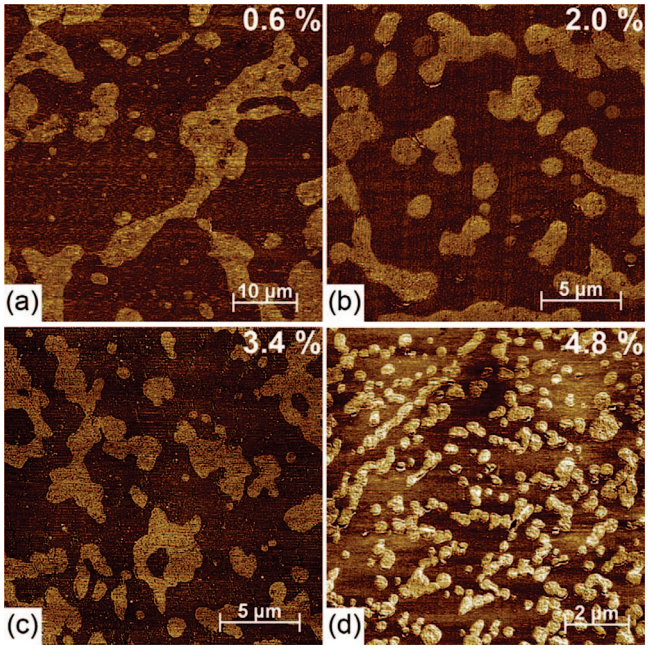

Figure 13. Atomic force micrographs of the compatibilized PA 6/SAN 30/70 blends with (a) 0.6 wt %, (b) 2.0 wt %, (c) 3.4 wt %, and (d) 4.8 wt % SANMA after compression molding.

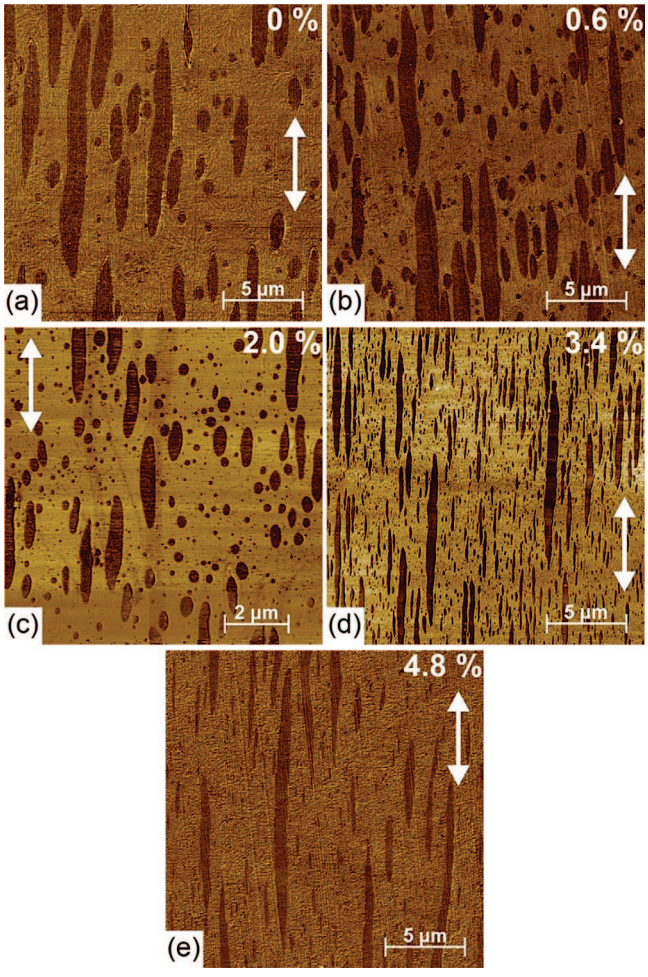

Figure 14. Atomic force micrographs of the PA 6/SAN 70/30 blends with (a) 0 wt %, (b) 0.6 wt %, (c) 2.0 wt %, (d) 3.4 wt %, and (e) 4.8 wt % SANMA. The samples were elongated to $\varepsilon_{max} = 1.8$ with $\dot{\varepsilon}_0 = 0.3\ s^{-1}$ at $T = 240$ °C. The direction of stretching is indicated by an arrow.

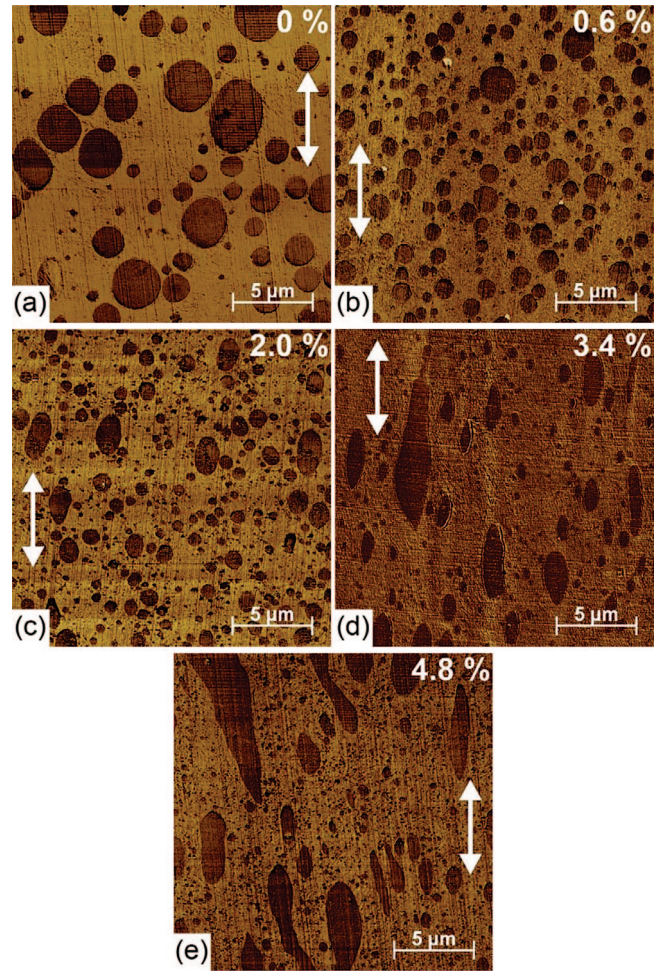

Figure 15. Atomic force micrographs of the PA 6/SAN 70/30 blends with (a) 0 wt %, (b) 0.6 wt %, (c) 2.0 wt %, (d) 3.4 wt %, and (e) 4.8 wt % SANMA at recovery time $t' = 10$ s (arrow = stretching direction). The elongation parameters are the same as in Figure 14. After elongation, the externally applied stress was zero and the samples could recover freely.

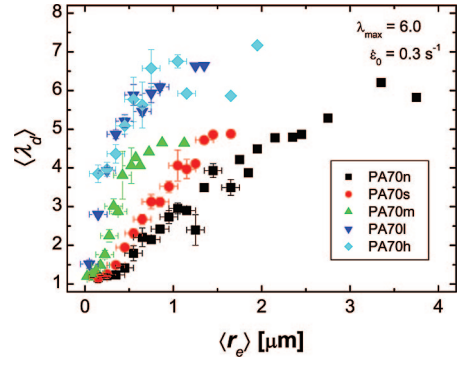

Figure 16. Stretch ratio λ_d of the SAN drops in the PA 6 matrix as a function of the equivalent radius r_e for the PA70 blends in Figure 14. See text for details. The elongation parameters were $\dot{\varepsilon}_0 = 0.3\ s^{-1}$, $\varepsilon_{max} = 1.8$, and $T = 240$ °C.

by measuring the major axis a' and the minor axis b' of the elliptical cross sections. Assuming that the drop is uniformly deformed such that λ_d is independent of the plane of cross section, the stretch ratio is given by

$$\lambda_d = (a'/b')^{2/3} \tag{6}$$

Figure 16 presents λ_d as a function of the equivalent radius $r_e = (a'b'^2)^{1/3}$ of a circle which has the same area as the elliptical

cross section. For each blend at least 100 elliptical cross sections were measured. The data points with error bars correspond to mean values $\langle\lambda_d\rangle$ which are averaged over elliptical cross sections with equivalent radii r_e in the interval $\langle r_e\rangle - 0.05\ \mu m < r_e < \langle r_e\rangle + 0.05\ \mu m$. Data points without error bars mark single measurements. The stretch ratio λ_d increases with increasing drop size. In addition, increasing the SANMA concentration from 0 to 3.4 wt % leads to a larger stretching ratio for the drops. However, a further increase to 4.8 wt % SANMA does not seem to change the stretch ratio of the drops anymore. The influence of the SANMA concentration on the interfacial tension driven retraction of the deformed droplets during recovery after elongation to $\varepsilon_{max} = 1.8$ with $\dot{\varepsilon}_0 = 0.3\ s^{-1}$ is depicted in Figure 15. The comparison of the stretch ratio of the drops of the different blends qualitatively demonstrates that the time scale for the interfacial tension driven recovery of the deformed drops increases with increasing SANMA concentration.

Discussion

Rheology. The emulsion model of Palierne with a constant interfacial shear modulus β_{20} has proven to be adequate for the analysis of linear viscoelastic data of physically compatibilized polymer blends.[16,37,38] The complex modulus $G^*(\omega)$ of an emulsion in the Palierne model is given by

$$G^*(\omega) = G^*_m(\omega)\frac{1 + 3/2\sum_i \phi_i \frac{E_i(\omega)}{D_i(\omega)}}{1 - \sum_i \phi_i \frac{E_i(\omega)}{D_i(\omega)}} \tag{7}$$

where

$$E_i(\omega) = 2[G^*_d(\omega) - G^*_m(\omega)][16G^*_m(\omega) + 19G^*_d(\omega)] + \frac{32\beta_{20}\alpha}{R_i^2} + \frac{8\alpha}{R_i}[2G^*_m(\omega) + 5G^*_d(\omega)] + \frac{4\beta_{20}}{R_i}[8G^*_m(\omega) + 13G^*_d(\omega)] \tag{8}$$

and

$$D_i(\omega) = [3G^*_m(\omega) + 2G^*_d(\omega)][16G^*_m(\omega) + 19G^*_d(\omega)] + \frac{32\beta_{20}\alpha}{R_i^2} + \frac{40\alpha}{R_i}[G^*_m(\omega) + G^*_d(\omega)] + \frac{4\beta_{20}}{R_i}[12G^*_m(\omega) + 13G^*_d(\omega)] \tag{9}$$

hold. In eqs 7–9, the quantity α denotes the interfacial tension between PA 6 and SAN, φ_i the volume fraction of drops with radius R_i, and G^*_m and G^*_d the complex modulus of matrix and dispersed phase, respectively. The prediction of the Palierne model was calculated for the uncompatibilized PA70n blend using the value $\alpha = 4.4$ mN/m (see ref 39) and setting $\beta_{20} = 0$. The volume fractions ϕ_i and drop radii R_i were determined from the drop size distribution of Figure 11.

Figure 17 presents the data of the uncompatibilized PA70n blend and the prediction of the Palierne model. At large frequencies the agreement between model and data is good. Although the G' data do not show the distinct shoulder at low ω which is predicted by the model, the agreement between model and data is satisfactory even at low ω. In order to account for the effect of compatibilization, we fitted eq 7 to the data of the reactively compatibilized blends by adjusting the interfacial tension α and the interfacial shear modulus β_{20}; see Figure 17. Especially for the larger SANMA concentration the extended Palierne model does not describe the enhanced moduli at large ω and does not seem adequate to describe the low frequency dependence of the dynamic moduli of our compatibilized blends.

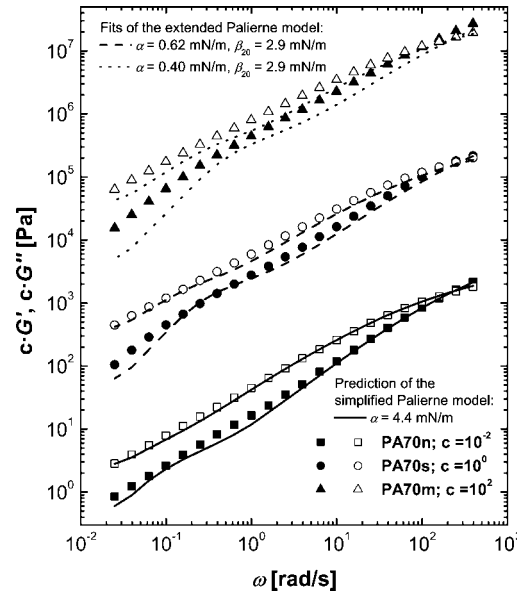

Figure 17. Comparison of the data of the PA70n blend with the Palierne model and comparison of the data of the PA70s and PA70m blend with the extended Palierne model. The data were multiplied by the factor c which is indicated in the figure. The filled symbols denote G' and the open symbols G''.

These results, in particular the increase of the dynamic moduli at larger frequencies, give evidence that already at low SANMA concentrations the compatibilizing reaction does not only change the properties of the polymer−polymer interface but considerably alters the relaxation behavior of the bulk.

With increasing SANMA concentration the linear viscoelastic properties of the blends change from an emulsion type behavior to a power law behavior in G' and G''. At the largest SANMA concentration, G' and G'' display over a frequency range of almost two decades a power law behavior with

$$G' \propto G'' \propto \omega^n \tag{10}$$

and a constant loss tangent $\tan\delta_c \approx 1.3$.

The scaling relation eq 10 does not differ much from the relation $G' = G'' \propto \omega^{0.5}$ of the Rouse model.[40] Such types of curves were first observed for block copolymers in the microphase separated state[41] and for critical gels,[42] but they have not been reported to our knowledge before for reactively compatibilized blends. The values of the relaxation exponent $n \approx 0.58$ and the constant value of the loss tangent $\tan\delta_c \approx 1.3$ fulfill the condition for the gelation point:[42]

$$\tan\delta_c = \tan\frac{n\pi}{2} \tag{11}$$

or $\delta_c = n\pi/2$. In general, these relaxation patterns occur in the vicinity of the liquid−solid transition (LST) and are a universal feature of the LST (i.e., the gelation of chemically cross-linking polymers, the physical gelation of microphase separating block copolymers, and of suspensions at the percolation threshold).[43] They can be understood by a long-range connectivity of molecular motion which is associated with a coupling of relaxation modes over a wide range of time scales.

At large SANMA concentrations an increasing portion of PA 6 chains is grafted to SANMA ($r = 0.34$ for PA70h; cf. Table 2). Thereby the effective volume fraction of the dispersed phase increases and the effective volume fraction of the matrix phase decreases. The grafted PA 6 chains are attached to SAN domains with a diameter being predominantly smaller than 0.5 μm (see Figure 10e). The very large number of the micellar-like SAN domains and at the same time a decreasing number

of unreacted PA 6 chains facilitate molecular interactions between the grafted PA 6 chains of neighboring SAN domains which possibly yields to the long-range connectivity between the domains as mentioned above.

In melt elongation, the PA70 blends with a SANMA concentration equal or smaller than 2.0 wt % depict the typical behavior of a linear viscoelastic liquid whereas at larger SANMA concentrations the elongational viscosity of the blends exceeds the linear viscoelastic prediction. Obviously, deformation processes occur in melt elongation which are not probed by small amplitude shear oscillations. These nonlinear effects occur for the blends which show at harmonic shear oscillations the limiting behavior of the LST. Consequently, the nonlinear deformation behavior in elongation possibly is strongly correlated to long-range interactions between the micellar-like SAN domains.

In recovery after melt elongation, the PA70n, the PA70s, and the PA70m blend display a time dependence of λ_r which is typical for emulsions.[27,28,44] The small instantaneous recovery of the blends can be explained by the very low molecular recovery portion of the pure components.[21] The subsequent increase of λ_r is associated with the interfacial tension driven recovery which causes the retraction of the deformed SAN droplets to a spherical shape (see Figure 14). For 20 s $< t' <$ 200 s, an intermediate plateau of λ_r appears, which indicates that at this stage the morphological recovery is almost completed (cf. Figure 15a−c). The plateau value of λ_r does not depend systematically on the SANMA concentration which can be explained by two competing effects. On the one hand, the stretch ratio of drops of the same size increases with SANMA concentration (cf. Figure 16) which leads to a larger recovered stretch of the sample. On the other hand, the average drop size decreases with SANMA concentration. These smaller drops are less deformed under the same hydrodynamic conditions, causing a reduction of the recovered stretch of the sample. Since the drops are deformed to a smaller stretch ratio for $\dot{\varepsilon}_0 = 0.1\ s^{-1}$ than for $\dot{\varepsilon}_0 = 0.3\ s^{-1}$, the effect of the morphology becomes less visible at lower $\dot{\varepsilon}_0$. Consequently, the transient recovered stretch increases to smaller values and the plateau of λ_r is less developed for $\dot{\varepsilon}_0 = 0.1\ s^{-1}$ than for $\dot{\varepsilon}_0 = 0.3\ s^{-1}$. For $t' > 200$ s the recovered stretch λ_r increases which is caused by the dominating effect of the surface tension between the sample and the nitrogen atmosphere. This increase depends on the viscosity of the sample and becomes mostly pronounced for the low viscous PA70n blend.

For the blends with a large SANMA concentration a different recovery behavior is observed. The blends display already at very low t' a considerable recovered stretch that strongly increases for $t' < 100$ s. At large t', the recovered stretch λ_r of the PA70l and PA70h blend depict a concave shape which indicates that the surface tension induced recovery portion is very small for these blends because of the large viscosity at small ω and large t, respectively (see Figure 3). For the PA70h blend, the elongational deformation at $\dot{\varepsilon}_0 = 0.3\ s^{-1}$ is almost completely reversible, similar to a viscoelastic solid. The fundamentally different recovery behavior of the blends at small and large SANMA concentrations confirms the previous assumption that the rheology of these blends is strongly influenced by additional mechanisms which dominate at large SANMA concentrations.

The linear viscoelastic behavior of the reactively compatibilized blends with 30 wt % PA 6 fundamentally differs from the behavior of the PA70 blends. All reactively compatibilized blends display a convex shape of the log G' vs log ω curve and a local maximum in tan δ. Such a behavior is frequently observed for suspensions where particle−particle interactions lead to the formation of network-like structures[45,46] and cannot be explained by the emulsion model.[47] The (compared to the SAN matrix) more viscous PA 6 droplets aggregate and partially coalesce to nonspherical clusterlike shaped domains. In analogy to suspensions with interacting particles the solid-like low frequency behavior of the blend can be interpreted by the network-like structure of PA 6 domains which is formed through attractive interactions between the grafted shells of neighboring domains.

In elongation all blends with 30 wt % PA 6 behave linearly viscoelastic at small strains. At larger strains the elongational viscosity increases more rapidly and exceeds the linear viscoelastic prediction. The onset of this strain-hardening like behavior is shifted toward lower strains with increasing SANMA concentration. Since the single blend components do not show strain-hardening,[21] the origin of this strain-hardening like behavior is related to the two-phase structure of blend. The enhancement of strain-hardening with larger SANMA concentration can be related to the nonlinear deformation of the intrinsic network between the PA 6 domains which becomes more resistive with increasing SANMA concentration. In recovery after elongation, the PA30 blends display a very different behavior, which depends on their SANMA concentration. The recovery dynamics of the neat blend is phenomenologically very similar to pure SAN.[21] Apparently, the surface tension which attempts to minimize the free surface of the sample has a dominant effect on the recovery of the sample at large t'. The morphological contribution is of minor relevance which is explained by a reduced deformation of the larger viscous PA 6 domains in the lower viscous SAN matrix during elongational flow. With increasing SANMA concentration the recovery dynamics of the blends changes to a behavior which is similar to the PA70l and PA70h blend. In this case the elastic properties of these PA30 blends become clearly pronounced (as also seen in G' at low ω) and cause a recovery behavior which is similar to that of a viscoelastic solid. Therefore the surface tension driven flow is suppressed such that at large SANMA concentrations the blends almost attain an equilibrium value of λ_r for $t' > 1000$ s.

Microscopic Deformation. The influence of reactive compatibilization on the morphology development during elongation was analyzed by determining the stretch ratio λ_d of the SAN drops of the PA70 blends. The increase of drop deformation with increasing SANMA concentration is in accordance with experimental studies on the effect of compatibilization via diblock copolymers on drop deformation.[48] The increase of λ_d with SANMA concentration can be explained by a decreased interfacial tension and by the flow-induced accumulation of compatibilizer molecules at the drop tips as shown in ref 48. The fact that an increase of SANMA concentration from 3.4 to 4.8 wt % did not change the drop deformation indicates that already at 3.4 wt % SANMA the interface is saturated with multigrafted SANMA chains.

Figure 15 reveals that the recovery process of the deformed drops is slowed down with SANMA concentration. This result qualitatively agrees with recovery experiments after steady shear using blends which were compatibilized by block copolymers.[49] In relaxation experiments after simple elongation the time scale of the shape relaxation was also increased for blends that were compatibilized by block copolymers above the critical concentration of drop surface saturation.[50]

Conclusions

In this work, the influence of reactive compatibilization on the melt flow properties and morphology of PA 6/SAN blends with a disperse morphology and varying concentration of a reactive agent (a styrene–acrylonitrile maleic anhydride terpolymer) was systematically investigated. The SAN domains

of the blends with a PA 6 matrix are stable with respect to coalescence because of a steric repulsion between the compatibilized drops. This effect leads to a decrease of the drop size with increasing SANMA concentration. At large SANMA concentrations micellar-like SAN domains are preferentially formed during blending which strongly influence the rheology of the PA 6 matrix. These blends depict the power-law behavior $G' \propto G'' \propto \omega^n$ ($n = 0.58$) in linear viscoelastic shear oscillations, a nonlinear transient elongational viscosity, and a strongly enhanced elasticity in recovery. On the contrary, for the blends with a SAN matrix phase compatibilization does not prevent agglomeration but it delays the coalescence process which leads to a clusterlike shape of the SAN domains. The linear viscoelastic behavior of these blends is similar to the behavior of semidilute suspensions with interacting particles at large SANMA concentrations. In elongation and subsequent recovery, the extent of strain-hardening and the recoverable strain increases if the SANMA concentration is increased. The comparison of the morphological and rheological behavior of the blends with different composition ratios gives a clear evidence for asymmetric properties of the reactively compatibilized interface. This phenomenon originates from the comblike architecture of the in situ generated interfacial agent and leads to different kinds of interaction between the domains of the dispersed phase depending whether SAN or PA 6 forms the matrix phase.

Finally, the influence of reactive compatibilization on the deformation of the dispersed phase was studied for the blends with 70 wt % PA 6. The stretch ratio of the reactively compatibilized SAN drops in the PA 6 matrix was larger compared to the stretch ratio of the drops of the neat blends and increased with SANMA concentration. In recovery after simple elongation reactive compatibilization increased the time for the recovery of the domains of the dispersed phase to a spherical shape.

Acknowledgment. The authors thank very much Dr. M. Weber and Dr. H. Steininger (BASF AG, Ludwigshafen am Rhein, Germany) for very stimulating and helpful discussions and for the donation of the materials. Very valuable discussions with Professors J. Meissner and H. C. Öttinger are also gratefully acknowledged. The authors are thankful to W. Schmidheiny, F. Mettler, and J. Hostettler for their experimental support and to the Swiss National Science Foundation for financial support (Project No. 200021-103287).

References and Notes

(1) Utracki, L. A. *Polymer Alloys and Blends*, 2nd ed.; Hanser: Munich, 1989.
(2) Crist, B.; Nesarikar, A. R. *Macromolecules* **1995**, *28*, 890–896.
(3) Yu, W.; Zhou, C. X.; Inoue, T. *J. Polym. Sci., Part B: Polym. Phys.* **2000**, *38*, 2378–2389.
(4) Koning, C.; van Duin, M.; Pagnoulle, C.; Jerome, R. *Prog. Polym. Sci.* **1998**, *23*, 707–757.
(5) Paul, D. R.; Bucknall, C. B. *Polymer Blends: Volume 1: Formulation*, 2nd ed.; Wiley: New York, 2000.
(6) Macosko, C. W.; Jeon, H. K.; Hoye, T. R. *Prog. Polym. Sci.* **2005**, *30*, 939–947.
(7) Triacca, V. J.; Ziaee, S.; Barlow, J. W.; Keskkula, H.; Paul, D. R. *Polymer* **1991**, *32*, 1401–1413.
(8) Majumdar, B.; Keskkula, H.; Paul, D. R. *Polymer* **1994**, *35*, 3164–3172.
(9) Kudva, R. A.; Keskkula, H.; Paul, D. R. *Polymer* **2000**, *41*, 225–237.
(10) Silva, J.; Machado, A. V.; Maia, J. *Rheol. Acta* **2007**, *46*, 1091–1097.
(11) Bayram, G.; Yilmazer, U.; Xanthos, M. *Polym. Eng. Sci.* **2001**, *41*, 262–274.
(12) Shi, D.; Ke, Z.; Yang, J. H.; Gao, Y.; Wu, J.; Yin, J. H. *Macromolecules* **2002**, *35*, 8005–8012.
(13) Jafari, S. H.; Pötschke, P.; Stephan, M.; Warth, H.; Alberts, H. *Polymer* **2002**, *43*, 6985–6992.
(14) Palierne, J. F. *Rheol. Acta* **1990**, *29*, 204–214.
(15) Palierne, J. F. *Rheol. Acta* **1991**, *30*, 497–497.
(16) Riemann, R. E.; Cantow, H. J.; Friedrich, C. *Macromolecules* **1997**, *30*, 5476–5484.
(17) Jacobs, U.; Fahrländer, M.; Winterhalter, J.; Friedrich, C. *J. Rheol.* **1999**, *43*, 1495–1509.
(18) Asthana, H.; Jayaraman, K *Macromolecules* **1999**, *32*, 3412–3419.
(19) Moan, M.; Huitric, J.; Mederic, P.; Jarrin, J. *J. Rheol.* **2000**, *44*, 1227–1245.
(20) Huo, Y. L.; Groeninckx, G.; Moldenaers, P. *Rheol. Acta* **2007**, *46*, 507–520.
(21) Sailer, C.; Handge, U. A. *Macromolecules* **2007**, *40*, 2019–2028.
(22) Sailer, C.; Handge, U. A. *Macromol. Symp.* **2007**, *254*, 217–225.
(23) Majumdar, B.; Paul, D. R.; Oshinski, A. J. *Polymer* **1997**, *38*, 1787–1808.
(24) van Duin, M.; Machado, A. V.; Covas, J *Macromol. Symp.* **2001**, *170*, 29–39.
(25) Weber, M.; Heckmann, W.; Goeldel, A *Macromol. Symp.* **2006**, *233*, 1–10.
(26) Meissner, J.; Hostettler, J *Rheol. Acta* **1994**, *33*, 1–21.
(27) Handge, U. A.; Pötschke, P. *J. Rheol.* **2004**, *48*, 1103–1122.
(28) Handge, U. A.; Pötschke, R. *J. Rheol.* **2005**, *49*, 1553–1553.
(29) Magonov, S. N.; Reneker, D. H. *Annu. Rev. Mater. Sci.* **1997**, *27*, 175–222.
(30) Schiessel, H.; Metzler, R.; Blumen, A.; Nonnenmacher, T. F *J. Phys. A: Math. Gen.* **1995**, *28*, 6567–6584.
(31) Yoon, Y.; Borrell, M.; Park, C. C.; Leal, L. G. *J. Fluid Mech.* **2005**, *525*, 355–379.
(32) Goldsmith, P. L. *Br. J. Appl. Phys.* **1967**, *18*, 813–830.
(33) Gido, S. P.; Lee, C.; Pochan, D. J.; Pispas, S.; Mays, J. W.; Hadjichristidis, N. *Macromolecules* **1996**, *29*, 7022–7028.
(34) Kitayama, N.; Keskkula, H.; Paul, D. R. *Polymer* **2000**, *41*, 8053–8060.
(35) Freluche, M.; Iliopoulos, I.; Flat, J. J.; Ruzette, A. V.; Leibler, L. *Polymer* **2005**, *46*, 6554–6562.
(36) Handge, U. A.; Schmidheiny, W. *Rheol. Acta* **2007**, *46*, 913–919.
(37) Van Hemelrijck, E.; Van Puyvelde, P.; Velankar, S.; Macosko, C. W.; Moldenaers, P. *J. Rheol.* **2004**, *48*, 143–158.
(38) Van Hemelrijck, E.; Van Puyvelde, P.; Macosko, C. W.; Moldenaers, P. *J. Rheol.* **2005**, *49*, 783–798.
(39) Son, Y. *Polymer* **2001**, *42*, 1287–1291.
(40) Doi, M.; Edwards, S. F. *The Theory of Polymer Dynamics*; Clarendon: Oxford, U.K., 1986.
(41) Bates, F. S. *Macromolecules* **1984**, *17*, 2607–2613.
(42) Chambon, F.; Winter, H. H. *J. Rheol.* **1987**, *31*, 683–697.
(43) Winter, H. H.; Mours, M. Rheology of polymers near liquid-solid transitions. In *Neutron Spin Echo Spectroscopy Viscoelasticity Rheology*; **1997**; Vol. 134.
(44) Gramespacher, H.; Meissner, J. *J. Rheol.* **1997**, *41*, 27–44.
(45) Masuda, T.; Nakajima, A.; Kitamura, M.; Aoki, Y.; Yamauchi, N.; Yoshioka, A. *Pure Appl. Chem.* **1984**, *56*, 1457–1475.
(46) Fahrländer, M.; Bruch, M.; Menke, T.; Friedrich, C. *Rheol. Acta* **2001**, *40*, 1–9.
(47) Bardollet, P.; Bousmina, M.; Muller, R *Polym. Adv. Technol.* **1995**, *6*, 301–308.
(48) Hu, Y. T.; Pine, D. J.; Leal, L. G. *Phys. Fluids* **2000**, *12*, 484–489.
(49) Wang, J.; Velankar, S. *Rheol. Acta* **2006**, *45*, 741–753.
(50) Mechbal, N.; Bousmina, M. *Macromolecules* **2007**, *40*, 967–975.

MA800200T